HHS Public Access

Author manuscript

ACS Nano. Author manuscript; available in PMC 2024 July 29.

Published in final edited form as:

ACS Nano. 2024 May 14; 18(19): 12477–12488. doi:10.1021/acsnano.4c02030.

Tunable Macroscopic Alignment of Self-Assembling Peptide Nanofibers

Adam C. Farsheed,
Department of Bioengineering, Rice University, Houston, Texas 77005, United States

Christian Zevallos-Delgado,
Department of Biomedical Engineering, University of Houston, Houston, Texas 77204, United States

Le Tracy Yu,
Department of Chemistry, Rice University, Houston, Texas 77005, United States

Sajede Saeidifard,

Corresponding Author: Jeffrey D. Hartgerink – *Department of Bioengineering, Rice University, Houston, Texas 77005, United States; Department of Chemistry, Rice University, Houston, Texas 77005, United States*; jdh@rice.edu.

Author Contributions

A.C.F. and J.D.H. conceived the study. A.C.F. performed all PLM, rheology, ATR-FTIR, SEM, 2D SAXS, cell seeding studies, live/dead and immunostaining, confocal imaging, data processing, including writing code and carrying out the quantification of actin and nuclear alignment, statistical analysis, and wrote the original manuscript draft. C.Z.D. performed OCE and completed data processing. L.T.Y. and C.C.C. prepared samples for Cryo-TEM and L.T.Y. performed all imaging. S.S. performed Brillouin microscopy and completed data processing. J.W.R.S. prepared samples and performed DLS. J.T.M. created all gelation baths and measured the sample diameter and swelling. A.J.T. synthesized and characterized K2. E.G.H. isolated VIC cells. K.J.G.A. oversaw the work of E.G.H. M.S. and K.V.L. oversaw the work of C.Z.D. and S.S. J.D.H. oversaw the work of A.C.F., L.T.Y., J.W.R.S., J.T.M., A.J.T., and C.C.C. All authors reviewed and edited the manuscript.

Notes

A preprint of this manuscript was deposited at bioRxiv with DOI: 10.1101/2024.02.02.578651.

The authors declare the following competing financial interest(s): A.C.F. and J.D.H. are listed as co-inventors on pending U.S. patent application #63/510,818. K.V.L. and M.S. have a financial interest in ElastEye LLC, which is not directly related to this work. The remaining coauthors declare they have no competing interests.

Complete contact information is available at: https://pubs.acs.org/10.1021/acsnano.4c02030

ASSOCIATED CONTENT

Supporting Information

The Supporting Information is available free of charge at https://pubs.acs.org/doi/10.1021/acsnano.4c02030.

K2 characterization (Figure S1), K2 concentration screen (Figure S2), precursor solution equilibration (Figure S3), precursor solution temperature screen (Figure S4), gelation bath composition screen (Figure S5), precursor solution extrusion rate screen (Figure S6), gelation bath phosphate buffer screen (Figure S7), effect of high ionic strength without increased phosphate anions (Figure S8), bulk K2 hydrogel geometry (Figure S9), optical coherence elastography system schematic (Figure S10), stiffness of aligned K2 hydrogels (Figure S11), Brillouin shift profiles for 5× PB hydrogels (Figure S12), VIC cell viability on K2 hydrogels (Figure S13), C2C12 cell viability on K2 hydrogels (Figure S14), C2C12 cell spreading on K2 hydrogels (Figure S15), C2C12 cell differentiation on K2 hydrogels (Figure S16), VIC cell spreading on small diameter K2 hydrogels (Figure S17), C2C12 cell spreading on small diameter K2 hydrogels (Figure S18), K2 hydrogel swelling (Figure S19) (PDF)

Hydrogel fabrication (Movie S1) (MP4)

Hydrogel fabrication PLM (Movie S2) (MP4)

Pre-gelled K2 hydrogel pick up (Movie S3) (MP4)

1× PB K2 hydrogel pick up (Movie S4) (MP4)

5× PB K2 hydrogel large pick up (Movie S5) (MP4)

5× PB K2 hydrogel small pick up (Movie S6) (MP4)

Pre-gelled K2 hydrogel OCE (Movie S7) (MP4)

1× PB K2 hydrogel OCE (Movie S8) (MP4)

3× PB K2 hydrogel OCE (Movie S9) (MP4)

5× PB K2 hydrogel OCE (Movie S10) (MP4)

Department of Biomedical Engineering, University of Houston, Houston, Texas 77204, United States

Joseph W. R. Swain,
Department of Chemistry, Rice University, Houston, Texas 77005, United States

Jonathan T. Makhoul,
Department of Bioengineering, Rice University, Houston, Texas 77005, United States

Department of Chemistry, Rice University, Houston, Texas 77005, United States

Adam J. Thomas,
Department of Chemistry, Rice University, Houston, Texas 77005, United States

Carson C. Cole,
Department of Chemistry, Rice University, Houston, Texas 77005, United States

Eric Garcia Huitron,
Department of Bioengineering, Rice University, Houston, Texas 77005, United States

Kathryn Jane Grande-Allen,
Department of Bioengineering, Rice University, Houston, Texas 77005, United States

Manmohan Singh,
Department of Biomedical Engineering, University of Houston, Houston, Texas 77204, United States

Kirill V. Larin,
Department of Biomedical Engineering, University of Houston, Houston, Texas 77204, United States

Jeffrey D. Hartgerink
Department of Bioengineering, Rice University, Houston, Texas 77005, United States

Department of Chemistry, Rice University, Houston, Texas 77005, United States

Abstract

Progress in the design and synthesis of nanostructured self-assembling systems has facilitated the realization of numerous nanoscale geometries, including fibers, ribbons, and sheets. A key challenge has been achieving control across multiple length scales and creating macroscopic structures with nanoscale organization. Here, we present a facile extrusion-based fabrication method to produce anisotropic, nanofibrous hydrogels using self-assembling peptides. The application of shear force coinciding with ion-triggered gelation is used to kinetically trap supramolecular nanofibers into aligned, hierarchical macrostructures. Further, we demonstrate the ability to tune the nanostructure of macroscopic hydrogels through modulating phosphate buffer concentration during peptide self-assembly. In addition, increases in the nanostructural anisotropy of fabricated hydrogels are found to enhance their strength and stiffness under hydrated conditions. To demonstrate their utility as an extracellular matrix-mimetic biomaterial, aligned nanofibrous hydrogels are used to guide directional spreading of multiple cell types, but strikingly, increased matrix alignment is not always correlated with increased cellular alignment. Nanoscale observations reveal differences in cell–matrix interactions between variably aligned scaffolds and

implicate the need for mechanical coupling for cells to understand nanofibrous alignment cues. In total, innovations in the supramolecular engineering of self-assembling peptides allow us to decouple nanostructure from macrostructure and generate a gradient of anisotropic nanofibrous hydrogels. We anticipate that control of architecture at multiple length scales will be critical for a variety of applications, including the bottom-up tissue engineering explored here.

Graphical Abstract:

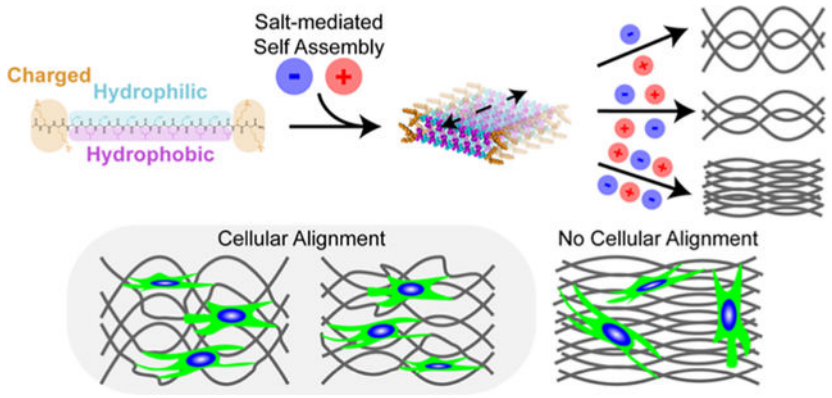

Keywords

self-assembling peptides; hydrogels; supramolecular chemistry; biomaterials; anisotropic tissue engineering

Fibrous proteins that comprise the extracellular matrix (ECM) of anisotropic, or directionally dependent, tissues guide cellular growth and organization.[1,2] Naturally, scientists and engineers have aimed to fabricate aligned fibrous scaffolds to direct cellular organization.[3,4] Fiber spinning techniques, such as electrospinning[5–7] (with the recent addition of rotary jet spinning[8]), have primarily been used toward this goal, representing a bottom-up approach, where individual fibers are deposited onto a rotating mandrel to form an aligned matrix. These methods, though, require specialized equipment, commonly involve the use of toxic solvents, and have difficulty recreating hierarchical three-dimensional (3D) geometries. Alternatively, top-down extrusion-based techniques that exert shear forces onto flowing extrudates have successfully been used to align biopolymers, such as collagen,[9–11] but biologically derived materials suffer from batch-to-batch variability, have sustainable sourcing concerns, and are difficult to chemically modify.[12] Similar shear-based strategies involving synthetic materials have relied on two component systems, where preformed fibers have been embedded into hydrogels prior to extrusion.[13–15] These materials, though, do not accurately recapitulate the fibrous nanostructure or chemical complexity of native ECM.

Self-assembling peptides, which rely on supramolecular mechanisms for assembly, represent a synthetical class of fibrous, ECM-mimetic biomaterials that have the benefits of design flexibility, biocompatibility, and chemical purity.[16,17] A longstanding goal within the field of supramolecular chemistry has been to follow a biomimetic route starting at molecular

design and resulting in macroscopic, hierarchical fibrous alignment.[18–20] Toward this goal, the extrusion of annealed peptide amphiphile (PA) solutions into ionic gelation baths has been shown to form aligned monodomain gels.[21] This technique has been replicated with a variety of other self-assembling peptide systems, indicating the generalizability of this strategy toward inducing macroscopic nanofibrous alignment.[22–25] In addition, this shear force-based alignment paradigm has been adapted to several scalable fabrication techniques, including extrusion 3D printing,[26,27] microfluidic chips,[28] and droplet inkjet printing.[29] Indeed, nanofibrous topography cues from peptide fibers have been shown to induce cellular alignment,[21,23,27–29] while the surface coating of PAs on PTFE-rubbed surfaces has also been shown as a robust strategy to guide cellular alignment.[30,31] Still, previously designed systems have not possessed a mechanism by which macroscopic nanofibrous alignment can be tuned and have primarily been characterized as having a binary switch between isotropy and anisotropy. This has limited the design space of anisotropic self-assembling peptide hydrogels and hampered their optimization for biological applications.

Here, we synthetically fabricate aligned nanofibrous hydrogels with tunable alignments using a β-sheet-forming peptide called "K2" with sequence $K_2(SL)_6K_2$ (Figure S1). Designed in our lab over a decade ago,[32] K2 is part of the multidomain peptide (MDP) family of assemblers.[33,34] The amphiphilic repeat of K2 drives β-sheet formation via hydrophobic packing of the leucine residues reinforced by backbone hydrogen bonding, whereas charge–charge repulsion at each termini opposes assembly. The delicate balance of these competing interactions allows ionic strength to act as a self-assembly trigger. At low ionic strength conditions, a small number of K2 monomers dimerize, a small number of nanofibers form, and the solution remains a liquid. At high ionic strength conditions, charge screening of the lysine residues allows for widespread β-sheet nanofiber formation and a bulk transition to a hydrogel (Figure 1A).

K2 forms a viscoelastic, shear-thinning hydrogel when dissolved in a physiological buffer, but counterintuitively, it does not gain anisotropic properties when sheared.[35] A mechanism explaining this phenomenon with self-assembling β-hairpin peptides has been investigated, in which fibrous domains fracture and recover under shear without affecting fibrillar alignment.[36] Therefore, we decoupled the hydrogel formation process into two components: (1) A precursor solution containing K2 dissolved in Milli-Q water and (2) a gelation bath containing salts and a buffer component. The extrusion of the precursor solution into the gelation bath provides the necessary counterions for K2 nanofibrillar formation and the bulk transition from a liquid to a hydrogel (Movie S1). We imaged this process with polarized light microscopy (PLM) and observed birefringence within the resulting hydrogel, suggestive of structural anisotropy (Movie S2). In this work, we demonstrate how the gelation bath composition determines K2 nanofibrous alignment, correlate hydrogel structural differences with bulk mechanical properties, and use this biomaterial system to better understand directed cellular spreading.

RESULTS AND DISCUSSION

Investigation of Alignment Parameters.

We initially sought to understand how the precursor solution's K2 concentration influences the resulting hydrogel's properties. Using a standard 100–1000 μL pipette tip and a phosphate-buffered saline (PBS) gelation bath, PLM revealed that no hydrogel formed using a 1 wt % K2 precursor solution and that an unstable amorphous hydrogel with slight birefringence formed using a 2 wt % K2 precursor solution (Figure S2A,B). In contrast, the use of 3 or 4 wt % K2 precursor solutions resulted in cylindrical, birefringent hydrogels (Figure S2C,D). These data suggest that K2 must be above a concentration threshold to form a robust, birefringent hydrogel, which is consistent with previously reported liquid crystalline behavior in other self-assembling peptide systems.[20]

While performing this study using a 3 wt % K2 precursor solution, we observed an unexpected increase in viscosity over time when stored at 4 °C (Figure S3A). Cryogenic transmission electron microscopy (Cryo-TEM) revealed that K2 nanofiber density increased after 1 day at 4 °C, suggesting that the supramolecular equilibration in this system is on the order of days (Figure S3D). Further supporting these findings, attenuated total reflectance Fourier transform infrared spectroscopy (ATR-FTIR) showed an increase in the amide I band at 1616 cm^{-1}, corresponding to C ▫ O stretching within the β-sheet (Figure S3B). In addition, dynamic light scattering (DLS) showed a significant increase in particle size between day 0 and day 1 (Figure S3C). Further analysis of the 3 wt % K2 precursor solution at day 21 revealed that an equilibrium had been reached by day 7 (Figure S3A–C). To further investigate the effect of temperature on this equilibration, 3 wt % K2 precursor solutions were stored at 4 °C, room temperature (~20 °C), and 37 °C, and their viscosity was measured over 7 days (Figure S4). While precursor solutions stored at 4 °C took a full 7 days before reaching an equilibrium viscosity (Figure S4A), those stored at room temperature took 3 days (Figure S4B) and those stored at 37 °C took just over 1 day (Figure S4C). Thus, precursor solution storage temperature had a significant effect on the time taken to reach equilibrium, while higher temperatures accelerated the process. This suggests that the observed behavior is a combined effect from both aging and molecular motion. We decided to use 3 wt % K2 that had been allowed to equilibrate at 4 °C for >7 days as the precursor solution for the remainder of the study.

Next, we examined how the gelation bath composition affects the resulting hydrogel's properties. Using a standard 0.1–10 μL pipette tip to screen a series of pH 7 gelation baths, PLM revealed a positive correlation between ionic strength and hydrogel birefringence (Figure S5). In addition, by manually lifting hydrogels from solution and observing if they fractured, a positive correlation between phosphate buffer concentration and hydrogel strength was found (Figure S5 checkmarks). Further implicating the importance of gelation bath composition, the precursor solution extrusion rate did not affect the observed birefringence pattern within the same gelation bath (Figure S6).

We were interested in further investigating differences between the 10 mM phosphate buffer/140 mM NaCl gelation bath, henceforth referred to as 1× PB, and the 50 mM phosphate buffer/140 mM NaCl gelation bath, henceforth referred to as 5× PB, due to them

leading to differences in hydrogel birefringence, strength, and being close in composition to phosphate-buffered saline (PBS) commonly used in cell culture. We therefore added 3× PB (30 mM phosphate buffer/140 mM NaCl, pH 7) and 10× PB (100 mM phosphate buffer/140 mM NaCl, pH 7) gelation baths to analyze a spectrum of phosphate buffer concentrations. In addition, a "pre-gelled" 3 wt % K2 unaligned control was included, in which 3 wt % K2 was dissolved in Hank's Balanced Salt Solution (HBSS) to form a hydrogel[35] and then extruded into 1× PB. PLM revealed a positive correlation between PB concentration and hydrogel birefringence at multiple extrusion diameters, although minor differences between groups were difficult to discern (Figure S7). We therefore used scanning electron microscopy (SEM) and two-dimensional small-angle X-ray scattering (2D SAXS) to carry out a more robust analysis of hydrogels extruded through a standard 100–1000 μL pipette tip (Figure 2). Regardless of alignment parameters, an expansive network of nanofibers was observed, while the PB concentration was qualitatively found to positively correlate with an increase in fiber alignment and packing (Figure 2B,C). In addition, close observation revealed an increase in nanofiber bundling as a function of PB concentration (Figure 2C). 2D SAXS quantitatively confirmed the trends observed via PLM and SEM, as the full width at half-maximum (fwhm) of the peak within the azimuthal distribution decreased from 71 to 61° to 53° between 1×, 3×, and 5× PB hydrogels, respectively (Figure 2D,E). Thus, we successfully engineered a self-assembling peptide system by which modest changes in phosphate buffer can be used to tune hierarchical nanofibrillar alignment (Figure 1A).

We were interested in investigating whether the observed fiber bundling was an effect of the high ionic strength within 5× PB, or specifically related to the higher concentration of multivalent phosphate anions within the gelation bath. We therefore fabricated a hydrogel using a 10 mM phosphate buffer/1400 mM NaCl, pH 7 gelation bath, and observed the fibers directly using SEM (Figure S8). While the fibers did possess alignment similar to 1× PB hydrogels, macroscopic fiber bundles were not observed. We concluded that the multivalent ions are necessary for fiber bundling, which is consistent with our previous work[37] and has also been observed in supramolecular collagen assembly.[38]

After seeing their effects on K2 nanofibrillar alignment, we were interested in understanding how the gelation bath composition affects bulk hydrogel geometry. We expected that hydrogel diameters would match the inner diameters of the tips used for extrusion (860 and 430 μm for 100–1000 and 0.1–10 μL pipette tips, respectively). This was true for pregelled hydrogels (813 and 440 μm), but the 1×, 3×, and 5× PB hydrogels followed an unexpected trend (Figure S9): 1× PB hydrogels were significantly larger (1156 and 618 μm), 3× PB hydrogels were similar (780 and 363 μm), and 5× PB hydrogels were significantly smaller (717 and 333 μm) when compared to pre-gelled hydrogels.

These data help elucidate a diffusion-mediated mechanism underlying the positive correlation between the PB concentration and K2 nanofibrillar alignment. Specifically, it helps in understanding what occurs between when the liquid K2 extrudate leaves the pipette tip and when phosphate ions within the gelation bath physically cross-link enough K2 nanofibers to initiate bulk gelation. We hypothesize that there are two competing diffusive interactions within the liquid extrudate during this time: (1) the outward diffusion of high-concentration K2 monomers toward the gelation bath and (2) the outward diffusion of water

molecules toward the high ionic strength gelation bath (dehydration). Macroscopically, 1 causes an increase in hydrogel diameter, whereas 2 causes a decrease in hydrogel diameter. Thus, as the PB concentration increases, the relative rate of 2 increases, which explains why hydrogels prepared in 1× (1 > 2), 3× (1 = 2), and 5× PB (1 < 2) gelation baths have declining diameters. In addition, this mechanism explains why the diameter of 5× PB hydrogels is smaller than the pipette tip inner diameter.

Considering why the PB concentration leads to the observed differences in nanoscale geometry, the greater 2 compared to 1, the higher nanofiber bundling and alignment is expected. This is in agreement with the mechanism for thermally mediated peptide amphiphile bundling and alignment,[21] which also implicates dehydration as the primary driver. Thus, although the shear forces present during extrusion are consistent regardless of PB concentration, higher alignment is achieved for higher PB concentrations. In total, we have established a self-assembly pathway to tune the macroscopic alignment of self-assembling peptide nanofibers.

Mechanical Characterization of Aligned Hydrogels.

We next wanted to understand how differences in fibrillar nanostructure affect the mechanical properties of K2 hydrogels. We hypothesized that greater nanofibrillar alignment, packing, and bundling would lead to stiffer K2 hydrogels. As K2 hydrogels are lifted from their gelation bath, hydrophilic cohesive forces counteract the hydrogel exiting the solution, and a downward tensile force is applied. We took advantage of this phenomenon to qualitatively compare the strength of K2 hydrogels fabricated into different gelation baths. Pre-gelled and 1× PB hydrogels cannot be removed from solution without fracturing (Movies S3 and S4), whereas 5× PB hydrogels (of large and small diameter) can be fully removed without fracture (Movies S5 and S6). These results were surprising, as only covalently cross-linked K2 hydrogels had previously been found to be strong enough to withstand removal from solution.[39] We therefore sought to further interrogate differences in mechanical properties between K2 gels.

In addition to being hydrated, the mechanical property regime of K2 hydrogels makes them challenging to characterize through most standard mechanical testing means. Further, the highly anisotropic nature of K2 hydrogels makes rheology an ineffective method for their characterization. As a result, we employed optical coherence elastography (OCE),[40] in which a 1 kHz noncontact microtap excitation was applied to one end of the cylindrical hydrogels, and the elastic wave speed was monitored as it propagated along the direction of nanofibrillar alignment (Figure S10). Using this method, we could maintain K2 hydration and determine quantitative differences in stiffness between samples. The average wave speed through pre-gelled unaligned hydrogels was measured to be 0.80 m/s (Figure 3A and Movie S7), which was not significantly different from 1× PB hydrogels, which had an average wave speed of 0.71 m/s (Figure 3B and Movie S8). In contrast, the average wave speeds through 3× and 5× PB hydrogels were computed to be 1.9 (Figure 3C and Movie S9) and 5.5 m/s (Figure 3D and Movie S10), respectively. Together, these data show a positive correlation between PB concentration and wave speed along the direction of nanofibrillar alignment (Figures 3F and S11). Assuming a constant density and using the Scholte wave model (see

the Methods section for detailed description),[41] the Young's moduli were calculated to be 2.0, 1.5, 11, and 99 kPa for the pre-gelled, 1×, 3×, and 5× PB hydrogels, respectively. If we assume that these hydrogels are isotropic, the pre-gelled and 1× PB hydrogels have stiffnesses similar to brain tissue, the 3× PB hydrogels have stiffnesses similar to striated muscle tissue, and the 5× PB hydrogels have stiffnesses similar to collagenous osteoid precursors of bone.[42,43]

We also imaged 5× PB hydrogels via Brillouin microscopy, which allows for an understanding of a material's bulk modulus at a given location.[44] We used this technique to understand how the hydrogel's mechanical properties vary radially approaching the neutral axis (Figure 3E). The Brillouin shift was found to increase as a function of the *Z*-axis (Figures 3E,G and S12), which suggests that the fiber alignment observed with SEM (Figure 2Biv) persists to the core. In addition, it agrees with the fact that shear forces during extrusion are the highest along the neutral axis. Robust characterization of aligned K2 hydrogels using OCE and Brillouin microscopy allows us to conclude that higher nanofibrillar alignment leads to stiffer hierarchical matrices.

Cellular Spreading on Aligned Hydrogels.

We hypothesized that cells would recognize and align along the direction of K2 nanofibrillar alignment and that higher scaffold alignment would better direct cellular alignment. Porcine valvular interstitial cells (VICs), which lie in aortic valve leaflets and are primarily responsible for secreting ECM, are known to respond to directional cues.[45–47] We seeded them onto pre-gelled, 1×, 3×, and 5× PB hydrogels and observed high cellular viability for up to 7 days (Figure S13). One day after seeding, confocal microscopy qualitatively revealed that VICs on 1×, 3×, and 5× PB hydrogels aligned along the direction of K2 nanofibrillar alignment, unlike the pre-gelled control (Figure 4A). Quantification of immunofluorescently labeled actin filaments (Figure 4Di) and cell nuclei (Figure 4Dii) corroborated these observations (see the Methods section for detailed description). VICs maintained this alignment trend at day 3 (Figure 4B,E), and by day 7, VICs on 1× and 3× PB hydrogels directionally grew to confluency (Figure 4C,F). Further, spreading patterns of VICs on 1× PB hydrogels at day 3 (Figure 4G) and day 7 (Figure 4H) show that these scaffolds promote macroscopic cellular alignment. Surprisingly, VICs on 5× PB hydrogels aligned no better than those on the pre-gelled control at day 7 (Figure 4Civ,F). These results suggested that greater nanofibrillar alignment had no benefit, and further, that matrices with extremely high alignments were not able to direct cell spreading (Figure 1B).

To corroborate these striking findings, we repeated this study using C2C12 cells, a murine myoblast cell line commonly used for skeletal muscle tissue engineering, which has also been shown to directionally align in response to mechanical cues.[10,48,49] K2 hydrogels again supported high viability (Figure S14) and at day 1 after seeding, myoblasts aligned along the direction of K2 nanofibrillar alignment on 1×, 3×, and 5× PB hydrogels (Figure S15A,D). While C2C12 cells on 1× and 3× PB hydrogels maintained this alignment trend at day 3, cells on 5× PB hydrogels instead exhibited similar spreading patterns to those on pre-gelled unaligned controls (Figure S15B,E). By day 7, myoblasts on 1× and 3× PB hydrogels directionally grew to confluency (Figure S15C,F) and staining of myosin heavy chain at day

14 revealed that some myoblasts spontaneously differentiated into aligned myotubes on 1× and 3× PB hydrogels (Figure S16B,C). In contrast, myoblasts on 5× PB hydrogels spread orthogonal to the direction of K2 nanofibers (Figure S15 Civ,Fii) and aligned myotubes were not observed at day 14 (Figure S16D).

To further verify these results, we repeated VIC and C2C12 seeding studies onto K2 hydrogel scaffolds with half the diameter, supposing that hydrogel curvature may be affecting cellular growth. However, the cellular spreading patterns matched the previously observed trend (Figures S17 and S18). Finally, we examined whether hydrogel swelling could account for these results, but no differences in diameter were observed for 5× PB hydrogels when incubated in cell culture media for up to a week (Figure S19). Thus, cells on 1× and 3× PB hydrogels elongated in the direction of nanofibrillar alignment, but higher scaffold anisotropy led to no observable improvements in directing cell spreading, and the highly aligned 5× PB hydrogels did not promote long-term cellular alignment (Figure 1B).

Subsequently, we imaged cellular spreading patterns via SEM to directly visualize how cells were interacting with the K2 matrices of varying alignments (Figure 5). Myoblasts and VICs were observed pulling on and becoming entangled in the 1× PB matrix (Figure 5A). In addition, both cell types were seen interacting with the 3× PB matrix similarly (Figure 5B), which was evident due to differences in matrix alignment directly next to, versus far from, cells (Figure 5Bii). Cells on the 5× PB matrix had drastically different appearances and were not seen pulling on or disrupting the highly aligned matrix (Figure 5C). Instead, cells appeared to be spreading as if they were on the 2D surface and astoundingly were even found to be spreading orthogonal to the direction of K2 nanofibrillar alignment (Figure 5Cii).

After directly observing cell–matrix interactions, we can hypothesize (1) why cells on 1× and 3× PB K2 hydrogels align similarly and (2) why cells on 5× PB K2 hydrogels do not align along K2 alignment. Because K2 nanofibers are <10 nm in diameter (Figure S3D), they are similar in size to individual integrins[50] and smaller than integrin clusters (~100 nm).[51,52] Previous work studying cell–matrix interactions using fibrous matrices has been limited to fibers greater than ~0.5 μm.[53–55] As a result, our system occupies an understudied length scale. Within our system, cells are seen pulling on the 1× and 3× PB matrices similarly (Figure 5A,B), and differences in alignment and packing do not seem to impede this cellular behavior. We hypothesize that this pulling is a visual representation of mechanical coupling between the cell body and the underlying matrix and is what allows cells to sense and elongate along scaffold anisotropy. Thus, for 1, we believe that differences in alignment and packing between 1× and 3× PB matrices do not lead to significant differences in cells being able to mechanically couple with the K2 nanofibrous network, and therefore, cells can sufficiently align on both matrices. In the case of 2, we believe that K2 nanofibrous packing and bulk stiffness are too high for cells to effectively pull at and mechanically couple with the fibrous network, and therefore, they cannot understand the mechanical alignment cues. While anisotropic fibrous matrices have previously been used to better understand aligned cell spreading,[54–56] the range of stiffnesses within the K2 hydrogel system surpasses those from previous studies due to increased fiber bundling and packing within more highly aligned K2 hydrogels. While K2 alignment and stiffness

cannot be decoupled, we can provide hypotheses for 1 and 2 that agree with the previously proposed "fiber recruitment" mechanism[53] and add to the body of literature, analyzing cell spreading behaviors on anisotropic fibrous matrices.

CONCLUSIONS

In conclusion, we have demonstrated an extrusion-based process using self-assembly to fabricate a macroscopic array of nanofibrous peptides. By coupling ion-triggered gelation with an applied shear force, we tuned nanostructural alignment based on self-assembly conditions. We rigorously characterized the structural and mechanical properties of the resulting hydrogels and gained insights into how nanostructural differences altered bulk hydrogel properties. To demonstrate one biomedical application of these materials, we examined the spreading behaviors of myoblasts and valvular interstitial cells on our nanofibrous matrices and observed directional cell growth reminiscent to that seen in the ECM of anisotropic tissues. Notably, cells were most favorably aligned when nanofiber alignment was moderate, supporting the need to have tunable control of these parameters. This work has broad implications for the design of future self-assembling peptide systems and how cell-instructive fibrous cues can be used for bottom-up tissue engineering.

METHODS

Peptide Synthesis and Purification.

FMOC-protected amino acids and low-loading rink amide MBHA resin were purchased from EMD Millipore (Burlington, MA). *O*-(7-Azabenzotriazol-1-yl)-*N*,*N*,*N*′,*N*′-tetramethyluronium hexafluorophosphate (HATU) was purchased from P3 BioSystems (Louisville, KY). *N*,*N*-dimethylformamide (DMF), dichloromethane (DCM), dimethyl sulfoxide (DMSO), piperidine, *N*,*N*-diisopropylethylamine (DiEA), acetic anhydride, trifluoroacetic acid (TFA), and diethyl ether were purchased from Fisher Scientific (Pittsburgh, PA). Piperidine, triisopropylsilane (TIPS), and anisole were purchased from Millipore Sigma (Burlington, MA).

K2 (full sequence: KKSLSLSLSLSLSLKK) was manually synthesized via solid-phase peptide synthesis. Each coupling followed the same process: 2, 5 min deprotections using 25% piperidine in DMF; 5, 30 s DMF washes; a ninhydrin test to confirm successful deprotection; a 20 min coupling using 4 equiv of amino acid and 4 equiv of HATU dissolved in 50% DMF/50% DMSO with 6 equiv of DiEA; 2, 1 min DCM washes; 2, 1 min DMF washes; and a ninhydrin test to confirm successful coupling. After coupling the last amino acid, one last deprotection was performed before acetylation of the N-terminus via 2, 45 min couplings using an excess of DiEA and acetic anhydride in DCM. Following 3, 1 min DCM washes, a ninhydrin test was used to confirm successful coupling. Peptide cleavage was performed for 3 h using TFA with Milli-Q water, TIPS, and anisole in excess as cleavage scavengers. TFA was then evaporated off using nitrogen gas, followed by trituration of the peptide in cold diethyl ether. Three cycles of centrifugation (10 min at 3400 RCF) followed by decanting of the supernatant were used to isolate the crude peptide. After allowing excess diethyl ether to evaporate overnight, the crude peptide was dissolved in Milli-Q water (0.5–1 wt %) and dialyzed against Milli-Q water for 4 days in 100–500 Da Spectra/Por Biotech

Cellulose Ester Dialysis Membranes (Spectrum Laboratories Inc. Rancho Dominguez, CA). Next, the peptide solutions were pH-adjusted to 7 and sterile-filtered using 0.2 μm cellulose acetate sterile syringe filters (VWR International, Radnor, PA) under sterile conditions. Finally, peptides were frozen overnight at −80 °C and lyophilized using a FreeZone 4.5 Liter Cascade Benchtop Freeze-Dry System (Labconco Corporation, Kansas City, MO) for 3 days, before being transferred to a −20 °C freezer for long-term storage. Peptide synthesis was confirmed (Figure S1) using a Bruker AutoFlex Speed MALDI ToF (Bruker Instruments, Billerica, MA).

Phosphate Buffer Gelation Baths.

For each gelation bath, the masses of monosodium phosphate monohydrate and disodium phosphate heptahydrate were calculated to achieve the desired phosphate buffer concentration at pH 7. The buffer components and NaCl were then dissolved in Milli-Q water and sterile-filtered using 0.2 μm cellulose acetate sterile syringe filters (VWR International, Radnor, PA) under sterile conditions.

Polarized Light Microscopy (PLM).

PLM was performed on an Eclipse E400 (Nikon Corporation, Tokyo, Japan) equipped with cross-polarizers. Images were captured on a mounted D7000 Digital Camera (Nikon Corporation, Tokyo, Japan) using a fixed exposure time and ISO. Samples were imaged on standard glass microscopy slides (Fisher Scientific, Pittsburgh, PA) at a consistent angle.

Rheology.

Rheology was performed using an AR-G2 rheometer (TA Instruments, New Castle, DE) equipped with a 12 mm parallel plate. 100 μL of 3% K2 in Milli-Q water was added to the stage and the plate was lowered to a gap of 500 μm. Excess solution was removed with a spatula and mineral oil was dripped around the stage to prevent dehydration of the sample during testing. Viscosity measurements were recorded during a shear sweep from 0.1 to 10 s^{-1}.

Cryo-Transmission Electron Microscopy (Cryo-TEM).

Cryo-TEM was performed using an FEI Tecnai F20 (FEI Company, Hillsboro, Oregon) equipped with a K2 summit camera (Gatan Inc., Pleasanton, CA). 3 wt % K2 in Milli-Q water was diluted in Milli-Q water to a final concentration of 0.1 wt % and added to glow-discharged Quantifoil CUR 1.2/1.3 400 mesh grids (Electron Microscopy Sciences, Hatfield, PA). Samples were then frozen using a Vitrobot Mark IV Plunge System (Thermo Fisher Scientific, Waltham, MA) and loaded into a 626 Single tilt liquid nitrogen cryo-transfer holder (Gatan Inc., Pleasanton, CA). Cryo-transmission electron micrographs were captured at 200 kV. Brightness and contrast have been consistently modified to aid in visualization.

Attenuated Total Reflectance Fourier Transform Infrared Spectroscopy (ATR-FTIR).

ATR-FTIR was performed using a Nicolet iS20 FT/IR spectrometer (Thermo Scientific, Waltham, MA) with a Golden Gate diamond window. Ten microliters of 3 wt % K2 in Milli-Q water was added onto the window and dried using nitrogen. Spectra consisted of 30

accumulations at a resolution of 4 cm^{-1} with background subtraction. To compare relative heights in the amide I band at 1616 cm^{-1}, spectra were normalized to the TFA peak at 1674 cm^{-1}.

Dynamic Light Scattering (DLS).

DLS was performed using a Malvern Zen 3600 Zetasizer (Malvern Instruments Ltd., Malvern, U.K.). Two microliters of 3 wt % K2 in Milli-Q water was diluted in Milli-Q water to a final concentration of 0.3 wt % and added to a disposable cuvette. *Z*-average and polydispersity index (PDI) were acquired using the default water parameters for all measurements.

Scanning Electron Microscopy (SEM).

SEM was performed using a Helios NanoLab 660 Scanning Electron Microscope (FEI Company, Hillsboro, OR). K2 hydrogel samples were transferred to Porous Spec Pots (Electron Microscopy Sciences, Hatfield, PA) and subjected to a series of ethanol in Milli-Q water dilutions (30, 50, 60, 70, 80, 90%, 2 × 100%), each for 10 min. Samples that also contained cells were fixed in 4% paraformaldehyde (Thermo Fisher Scientific, Waltham, MA) for 30 min prior to the serial dilution process. Next, samples were critical point dried using a Leica EM CPD300 (Leica Biosystems, Deer Park, IL) and coated with 5 nm of gold using a Denton Desk V Sputter System (Denton Vacuum, Moorestown, NJ). Scanning electron micrographs were captured at 1–2 kV, 25 pA, and were cropped and rotated so the direction of K2 nanofibrillar alignment was horizontal.

2D Small-Angle X-ray Scattering (2D SAXS).

2D SAXS was performed using a Rigaku S-MAX 3000 (Rigaku, Tokyo, Japan) at the University of Houston within the lab of Dr. Megan Robertson. K2 hydrogel samples were placed horizontally onto SpectroMembrane Polyimide 7.5 μm films (Chemplex Industries, Palm City, FL), mounted perpendicular to the X-ray path, and pulled to vacuum. After locating the X/Y location of maximum signal intensity, a 5 min X-ray exposure was performed on each sample. Following background subtraction, the exposure pattern was integrated over the azimuthal angle using 1° increments between the Q-range of 0.012–0.04 $Å^{-1}$. Data points corresponding to the following angles were omitted during plotting as they consistently presented large outliers: 1.5, 44.6, 88.7, 89.7, 90.8, 134.9, 152.9, 153.9, 177.9, 178.9, 180°.

Swelling Measurements.

After fabrication into their respective gelation baths using standard 100–1000 and 0.1–10 μL pipette tips (VWR International, Radnor, PA), K2 hydrogels were transferred to C2C12 growth media within a 12-well plate and stored in a 37 °C incubator. Hydrogels were imaged using an OMAX 18 MP USB 3.0 Digital Camera (OMAX Microscope) at each time point and all diameter measurements were performed manually in ImageJ (National Institutes of Health, Bethesda, MA).

Optical Coherence Elastography (OCE).

Figure S10 shows a schematic of the custom-built OCE system. Wave excitation was generated using a $7 \times 7 \times 42$ mm^3 Piezo Stack Actuator (PiezoDrive, Newcastle, Australia) attached to a needle that was placed in direct contact with the hydrogel surface. Wave propagation was detected using a phase-sensitive Optical Coherence Tomography (PhS-OCT) system with ~9 μm axial resolution (in air), ~8 μm transversal resolution, and 0.28 nm of displacement stability. The A-line acquisition was set to 25 kHz during OCE acquisition. The piezo stack was driven by 5 pulses at 1 kHz, which was generated by a DG4162 Waveform Generator (RIGOL Technologies, Suzhou, China) and amplified by a PDu150 Three-Channel 150 V piezo drive (PiezoDrive, Newcastle, Australia). The burst of the signal was synchronized with the OCT frame trigger during the M-B mode scan to scan 500 points over 2.5 mm laterally with each M-mode scan consisting of 500 A-lines.

OCE is the elastography extension of optical coherence tomography (OCT), where the A-line constitutes the depth information (z-axis) of a sample at a given lateral position. The A-line is complex-valued, where the magnitude represents the depth-dependent intensity of the backscattered light, and its phase can be used to track the tissue displacement induced by the excitation in the tissue.[57] For two consecutive moments (t_0 and t_1), where $t_0 < t_1$ at a particular lateral position (t_0) and where a certain number of A-lines were acquired over time, the backscattered light's axial temporal phase difference is $\Delta\varphi(z) = \varphi(z, t_1) - \varphi(z, t_2)$, and the particle velocity is calculated as $v_z(z, t) = \Delta\varphi(z, t)\lambda_0/(4\pi\Delta t)$, where Δt is the resolution time and λ_0 is the source central wavelength.[58] For all lateral positions, where in each of them, multiple A-lines were collected, the phase difference ($\Delta\varphi$) of the A-line complex values provides the particle velocity used to build spatiotemporal images.

Axial particle velocities (v_z) were calculated based on the depth-dependent phase (φ) difference between two consecutive A-line complex values, $v_z(z, t) = \Delta\varphi(z, t)\lambda_0/(4\pi\Delta t)$, using $n = 1.37$ as the refractive index for phosphate-buffered saline gelation baths,[59] $\Delta t \approx 40$ μs (temporal resolution), and $\lambda_0 = 840$ nm for the central wavelength of the OCT light source. Wave velocities were computed as the slope of the wave propagation on spatiotemporal images. Since K2 hydrogels were immersed in phosphate-buffered saline gelation baths, the scan and wave propagation areas were under liquid. Therefore, the Scholte wave model was used to describe the elastic properties of the hydrogels, where the shear wave velocity (C_s) is related to the Scholte wave speed (C_{sch}) by $C_{sch} = 0.846C_s$.[60] The Scholte Young's modulus (E) was calculated with the formula: $E = \left(3\rho/0.846^2\right) \times C_{sch}^2$, assuming a hydrogel density (ρ) of 1000 kg/m^3.[41] All calculations were performed in MATLAB 2020b (Mathworks Inc., Natick, MA).

Brillouin Microscopy.

The home-built Brillouin microscopy system was based on a two-stage virtually imaged phase array (VIPA) spectrometer. A single-mode 660 nm laser (Torus, Laser Quantum Inc., Fremont, CA) with an incident sample power of ~17 mW was utilized, and a microscope was placed coaxially with the system to align the sample. A 40× water immersion microscope objective with a 0.8 numerical aperture was used to focus the laser beam onto

the sample. The lateral resolution was ~1.8 μm and the axial resolution was ~2.3 μm. Before each experiment, calibration was performed using water, acetone, and methanol to acquire the spectral pixel resolution and the free spectral range. A 420 μm × 10 μm brillouin scan was taken with a step size of 1 μm. An electron-multiplying charged coupled device camera (iXon Andor, Belfast, U.K.) with an exposure time of 0.1 s was used to capture the backscattered light from the sample after passing through the VIPA-based spectrometer.

A program written in the LabVIEW 20.0.1 Development System (NI, Austin, TX) was used to synchronously control the CCD camera, 3D linear motorized stage, and data acquisition board. The obtained Brillouin spectrum was analyzed using a Lorentzian fit to determine the Brillouin frequency shift. During the measurement, the sample was translated in 3D with the prescribed step size. Over a window, the Brillouin spectrum was summed before fitting to enhance the signal-to-noise ratio.[61]

Cell Culture and Seeding.

Fresh hearts from male and female young adult pigs (6–9 months old) were acquired from a commercial abattoir (Animal Technologies, Tyler, TX).[62] The aortic valve cusps were dissected, soaked in 2.5% antibiotic/antimycotic solution (ABAM; stock concentration of 10,000 IU penicillin, 10,000 μg/mL streptomycin and 25 μg/mL amphotericin B; Corning, Corning, NY) in phosphate-buffered saline (PBS), and rinsed with PBS. The washing steps were repeated two times before the VICs were harvested following previously described methods.[46,63] Briefly, the tissue was first incubated in an enzymatic solution containing 2 mg/mL collagenase II (Worthington Biochemical, Lakewood, NJ) in HyClone Low Glucose Dulbecco's modified Eagle's medium (Cytiva, Marlborough, MA) supplemented with 2.5% ABAM for 30 min under gentle agitation at 37 °C. Next, the cusps were denuded of their endothelium before being minced and placed into an enzymatic mixture of 2 mg/mL collagenase III (Worthington Biochemical, Lakewood, NJ), 0.1 mg/mL hyaluronidase (Worthington Biochemical, Lakewood, NJ), and 2 mg/mL Dispase II (STEMCELL Technologies, Vancouver, Canada) for 4 h under gentle agitation at 37 °C. The VICs were isolated from the digested tissue using a 70 μm cell strainer, pelleted at 1500 RCF for 5 min, resuspended, and grown in 45% HyClone Low Glucose Dulbecco's modified Eagle's medium (Cytiva, Marlborough, MA) supplemented with 25 mM HEPES, 44% HyClone Ham's Nutrient Mixture F12 (Cytiva, Marlborough, MA), 10% Gibco Fetal Bovine Serum (Thermo Fisher Scientific, Waltham, MA), and 1% penicillin–streptomycin (Thermo Fisher Scientific, Waltham, MA). Frozen C2C12 myoblasts were purchased from ATCC (Manassas, VA) and were grown in 89% Gibco Dulbecco's modified Eagle's medium (Thermo Fisher Scientific, Waltham, MA) supplemented with high glucose, sodium pyruvate, L-glutamine, and phenol red, 10% Gibco Fetal Bovine Serum (Thermo Fisher Scientific, Waltham, MA), and 1% penicillin–streptomycin (Thermo Fisher Scientific, Waltham, MA). All cells were used between passages 1 and 4.

For cell seeding studies, K2 hydrogels were fabricated under sterile conditions before being transferred to PBS. They were then moved to 8-well high Bioinert μ-Slides (Ibidi, Grafelfing,¨ Germany) and placed into an incubator for 10 min prior to cell seeding. Cells were passaged to 200,000 cells/mL, PBS was removed from all wells to leave just the

K2 hydrogels, and 10,000 cells (100,000 cells for cell viability studies) were added to the bottom of each well. Finally, media were added to each well and the slides were moved back into the incubator. Media were replaced every day for the remainder of the study.

Staining and Imaging.

Cells on K2 hydrogels were stained with Calcein AM and ethidium homodimer (Thermo Fisher Scientific, Waltham, MA) following manufacturer protocols for cell viability studies. Imaging was performed using a Zeiss LSM800 Airyscan (Oberkochen, Germany) and the "3D objects counter" plugin within ImageJ (National Institutes of Health, Bethesda, MA) was used to count live and dead cells, before being exported to Microsoft Excel (Microsoft Corporation, Redmond, WA) for viability calculations.

Immunostaining of cells on K2 hydrogels followed the process: 3 PBS washes; 30 min fixation in 4 wt % paraformaldehyde (Thermo Fisher Scientific, Waltham, MA); 3 PBS washes; 10 min quenching with 100 mM glycine; 30 min permeabilization with 0.2% Triton-X (Fisher Scientific, Pittsburgh, PA) in PBS; 1 h blocking with 1% bovine serum albumin (Genetex, Irvine, CA)/0.2% Triton-X in PBS; 1 h staining with Alexa Fluor 488 Phalloidin (Thermo Fisher Scientific, Waltham, MA) diluted 1:400 in 1% BSA/0.2% Triton-X in PBS; 3 PBS washes; 10 min staining with DAPI (Thermo Fisher Scientific, Waltham, MA) diluted 1:500 in 1% BSA/0.2% Triton-X in PBS; 3 PBS washes; clearing and storage in 88% glycerol (Thermo Fisher Scientific, Waltham, MA). For immunostaining of C2C12 cell differentiation, myosin heavy chain (MF 20, DSHB, Iowa City, IA) was diluted 1:10 and used as the primary antibody and Goat Antimouse Alexa Fluor Plus 488 (Thermo Fisher Scientific, Waltham, MA) was diluted 1:500 and used as the secondary antibody. All imaging was performed on a Zeiss LSM800 Airyscan (Oberkochen, Germany) and maximum intensity projections of *z*-stacks were created in ImageJ (National Institutes of Health, Bethesda, MA). Collected images were cropped and rotated so the direction of K2 nanofibrillar alignment was always horizontal.

Quantification of Actin and Nuclear Alignment.

Unprocessed maximum intensity projections of immunofluorescently labeled actin filaments were imported into ImageJ (National Institutes of Health, Bethesda, MA) and the plugin OrientationJ[64] was used to locally determine the Fourier gradient structure tensor using a 2 pixel local window, a 5% minimum coherency, and a 5% minimum energy. The structure tensor was then imported into MATLAB 2023a (Mathworks Inc., Natick, MA) and the angle corresponding to the maximum value was shifted to be 0°. Next, a polar histogram was generated (which is displayed next to each confocal microscopy image) and the toolbox CircStat[65] was used to calculate the mean resultant vector length of the polar distribution, where 0 corresponds to isotropy and 1 to anisotropy, as has been previously published.[66]

Unprocessed maximum intensity projections of immunofluorescently labeled cell nuclei were imported into ImageJ (National Institutes of Health, Bethesda, MA) and the default automatic threshold was applied and converted to a mask. If the automated process failed, this step was performed manually. Next, the mask was dilated and eroded twice, and a watershed was applied. The Analyze Particle function was then used to find the angle of

each ellipse and was exported into MATLAB 2023a (Mathworks Inc., Natick, MA). Finally, the difference between each ellipse angle and the angle of K2 nanofibrillar alignment was calculated, similar to previously published methods.[13]

Statistical Analysis.

Prism 10 (GraphPad Software, Boston, MA) was used for all statistical analyses. Specifics about data plotted and statistical tests used are listed in all figure captions.

Supplementary Material

Refer to Web version on PubMed Central for supplementary material.

ACKNOWLEDGMENTS

The authors thank M. Robertson for access to the Rigaku S-MAX 3000 2D SAXS at the University of Houston and J. Hanson for training. They also thank B. Utama for help with confocal microscopy and Rice University's Biomaterials Lab. They thank J. Miller and J. Beckham for helpful discussions.

Funding

This work was supported in part by the National Institutes of Health grants R01DE021798 (to J.D.H.), R01EY022362 (to K.V.L.), R01HD095520 (to K.V.L.), R01EY030063 (to K.V.L.); the National Science Foundation grant 2129122 (to K.J.G.A.); the National Science Foundation Graduate Research Fellowship Program (to A.C.F., J.W.R.S., C.C.C.); and The Welch Foundation Research grant C-2141.

REFERENCES

(1). Frantz C; Stewart KM; Weaver VM The Extracellular Matrix at a Glance. J. Cell Sci. 2010, 123, 4195–4200. [PubMed: 21123617]

(2). Mouw JK; Ou G; Weaver VM Extracellular Matrix Assembly: A Multiscale Deconstruction. Nat. Rev. Mol. Cell Biol. 2014, 15, 771–785. [PubMed: 25370693]

(3). Xing J; Liu N; Xu N; Chen W; Xing D Engineering Complex Anisotropic Scaffolds beyond Simply Uniaxial Alignment for Tissue Engineering. Adv. Funct. Mater. 2022, 32, No. 2110676.

(4). Sano K; Ishida Y; Aida T Synthesis of Anisotropic Hydrogels and Their Applications. Angew. Chem., Int. Ed. 2018, 57, 2532–2543.

(5). Matthews JA; Wnek GE; Simpson DG; Bowlin GL Electrospinning of Collagen Nanofibers. Biomacromolecules 2002, 3, 232–238. [PubMed: 11888306]

(6). Yang F; Murugan R; Wang S; Ramakrishna S Electrospinning of Nano/Micro Scale Poly(L-Lactic Acid) Aligned Fibers and Their Potential in Neural Tissue Engineering. Biomaterials 2005, 26, 2603–2610. [PubMed: 15585263]

(7). Xu Y; Shi G; Tang J; Cheng R; Shen X; Gu Y; Wu L; Xi K; Zhao Y; Cui W; Chen L ECM-Inspired Micro/Nanofibers for Modulating Cell Function and Tissue Generation. Sci. Adv. 2020, 6, No. eabc2036. [PubMed: 33239291]

(8). Chang H; Liu Q; Zimmerman JF; Lee KY; Jin Q; Peters MM; Rosnach M; Choi S; Kim SL; Ardoña HAM; MacQueen LA; Chantre CO; Motta SE; Cordoves EM; Parker KK Recreating the Heart's Helical Structure-Function Relationship with Focused Rotary Jet Spinning. Science 2022, 377, 180–185. [PubMed: 35857545]

(9). Nerger BA; Brun P-T; Nelson CM Microextrusion Printing Cell-Laden Networks of Type I Collagen with Patterned Fiber Alignment and Geometry. Soft Matter 2019, 15, 5728–5738. [PubMed: 31267114]

(10). Nakayama KH; Quarta M; Paine P; Alcazar C; Karakikes I; Garcia V; Abilez OJ; Calvo NS; Simmons CS; Rando TA; Huang NF Treatment of Volumetric Muscle Loss in Mice Using Nanofibrillar Scaffolds Enhances Vascular Organization and Integration. Commun. Biol. 2019, 2, No. 170. [PubMed: 31098403]

(11). Giacomini F; Barata DB; Rho HS; Birgani ZT; van Blitterswijk C; Giselbrecht S; Truckenmüller R; Habibović P. Microfluidically Aligned Collagen to Maintain the Phenotype of Tenocytes in Vitro. Adv. Healthcare Mater. 2023, 13, No. e2303672.

(12). Aisenbrey EA; Murphy WL Synthetic Alternatives to Matrigel. Nat. Rev. Mater. 2020, 5, 539–551. [PubMed: 32953138]

(13). Choi S; Lee KY; Kim SL; MacQueen LA; Chang H; Zimmerman JF; Jin Q; Peters MM; Ardoña HAM; Liu X; Heiler A-C; Gabardi R; Richardson C; Pu WT; Bausch AR; Parker KK Fibre-Infused Gel Scaffolds Guide Cardiomyocyte Alignment in 3D-Printed Ventricles. Nat. Mater. 2023, 22, 1039–1046. [PubMed: 37500957]

(14). Prendergast ME; Davidson MD; Burdick JA A Biofabrication Method to Align Cells within Bioprinted Photo-crosslinkable and Cell-Degradable Hydrogel Constructs via Embedded Fibers. Biofabrication 2021, 13, No. 044108.

(15). Gladman AS; Matsumoto EA; Nuzzo RG; Mahadevan L; Lewis JA Biomimetic 4D Printing. Nat. Mater. 2016, 15, 413–418. [PubMed: 26808461]

(16). Du X; Zhou J; Shi J; Xu B Supramolecular Hydrogelators and Hydrogels: From Soft Matter to Molecular Biomaterials. Chem. Rev. 2015, 115, 13165–13307. [PubMed: 26646318]

(17). Cui H; Webber MJ; Stupp SI Self-Assembly of Peptide Amphiphiles: From Molecules to Nanostructures to Biomaterials. Pept. Sci. 2010, 94, 1–18.

(18). Whitesides GM; Grzybowski B Self-Assembly at All Scales. Science 2002, 295, 2418–2421. [PubMed: 11923529]

(19). Aida T; Meijer EW; Stupp SI Functional Supramolecular Polymers. Science 2012, 335, 813–817. [PubMed: 22344437]

(20). Yuan C; Ji W; Xing R; Li J; Gazit E; Yan X Hierarchically Oriented Organization in Supramolecular Peptide Crystals. Nat. Rev. Chem. 2019, 3, 567–588.

(21). Zhang S; Greenfield MA; Mata A; Palmer LC; Bitton R; Mantei JR; Aparicio C; de la Cruz MO; Stupp SI A Self-Assembly Pathway to Aligned Monodomain Gels. Nat. Mater. 2010, 9, 594–601. [PubMed: 20543836]

(22). Wall BD; Diegelmann SR; Zhang S; Dawidczyk TJ; Wilson WL; Katz HE; Mao H-Q; Tovar JD Aligned Macroscopic Domains of Optoelectronic Nanostructures Prepared via Shear-Flow Assembly of Peptide Hydrogels. Adv. Mater. 2011, 23, 5009–5014. [PubMed: 22180891]

(23). Sleep E; Cosgrove BD; McClendon MT; Preslar AT; Chen CH; Sangji MH; Pérez CMR; Haynes RD; Meade TJ; Blau HM; Stupp SI Injectable Biomimetic Liquid Crystalline Scaffolds Enhance Muscle Stem Cell Transplantation. Proc. Natl. Acad. Sci. U.S.A. 2017, 114, E7919–E7928. [PubMed: 28874575]

(24). Christoff-Tempesta T; Cho Y; Kim D-Y; Geri M; Lamour G; Lew AJ; Zuo X; Lindemann WR; Ortony JH Self-Assembly of Aramid Amphiphiles into Ultra-Stable Nanoribbons and Aligned Nanoribbon Threads. Nat. Nanotechnol. 2021, 16, 447–454. [PubMed: 33462430]

(25). Marshall LJ; Wallace M; Mahmoudi N; Ciccone G; Wilson C; Vassalli M; Adams DJ Hierarchical Composite Self-Sorted Supramolecular Gel Noodles. Adv. Mater. 2023, 35, No. e2211277. [PubMed: 36720202]

(26). Chin SM; Synatschke CV; Liu S; Nap RJ; Sather NA; Wang Q; Álvarez Z; Edelbrock AN; Fyrner T; Palmer LC; Szleifer I; de la Cruz MO; Stupp SI Covalent-Supramolecular Hybrid Polymers as Muscle-Inspired Anisotropic Actuators. Nat. Commun. 2018, 9, No. 2395. [PubMed: 29921928]

(27). Sather NA; Sai H; Sasselli IR; Sato K; Ji W; Synatschke CV; Zambrotta RT; Edelbrock JF; Kohlmeyer RR; Hardin JO; Berrigan JD; Durstock MF; Mirau P; Stupp SI 3D Printing of Supramolecular Polymer Hydrogels with Hierarchical Structure. Small 2021, 17, No. e2005743. [PubMed: 33448102]

(28). Sant S; Coutinho DF; Gaharwar AK; Neves NM; Reis RL; Gomes ME; Khademhosseini A Self-Assembled Hydrogel Fiber Bundles from Oppositely Charged Polyelectrolytes Mimic Micro-/Nanoscale Hierarchy of Collagen. Adv. Funct. Mater. 2017, 27, No. 1606273. [PubMed: 31885528]

(29). Hedegaard CL; Collin EC; Redondo-Gómez C; Nguyen LTH; Ng KW; Castrejón-Pita AA; Castrejón-Pita JR; Mata A Hydrodynamically Guided Hierarchical Self-assembly of Peptide–Protein Bioinks. Adv. Funct. Mater. 2018, 28, No. 1703716.

(30). Gouveia RM; Castelletto V; Alcock SG; Hamley IW; Connon CJ Bioactive Films Produced from Self-Assembling Peptide Amphiphiles as Versatile Substrates for Tuning Cell Adhesion and Tissue Architecture in Serum-Free Conditions. J. Mater. Chem. B 2013, 1, 6157–6169. [PubMed: 32261001]

(31). Gouveia RM; Hamley IW; Connon CJ Bio-Fabrication and Physiological Self-Release of Tissue Equivalents Using Smart Peptide Amphiphile Templates. J. Mater. Sci.: Mater. Med. 2015, 26, No. 242. [PubMed: 26411438]

(32). Aulisa L; Dong H; Hartgerink JD Self-Assembly of Multidomain Peptides: Sequence Variation Allows Control over Cross-Linking and Viscoelasticity. Biomacromolecules 2009, 10, 2694–2698. [PubMed: 19705838]

(33). Moore AN; Hartgerink JD Self-Assembling Multidomain Peptide Nanofibers for Delivery of Bioactive Molecules and Tissue Regeneration. Acc. Chem. Res. 2017, 50, 714–722. [PubMed: 28191928]

(34). Dong H; Paramonov SE; Aulisa L; Bakota EL; Hartgerink JD Self-Assembly of Multidomain Peptides: Balancing Molecular Frustration Controls Conformation and Nanostructure. J. Am. Chem. Soc. 2007, 129, 12468–12472. [PubMed: 17894489]

(35). Farsheed AC; Thomas AJ; Pogostin BH; Hartgerink JD 3D Printing of Self-Assembling Nanofibrous Multidomain Peptide Hydrogels. Adv. Mater. 2023, 35, No. e2210378. [PubMed: 36604310]

(36). Yan C; Altunbas A; Yucel T; Nagarkar RP; Schneider JP; Pochan DJ Injectable Solid Hydrogel: Mechanism of Shear-Thinning and Immediate Recovery of Injectable β-Hairpin Peptide Hydrogels. Soft Matter 2010, 6, 5143–5156. [PubMed: 21566690]

(37). Bakota EL; Sensoy O; Ozgur B; Sayar M; Hartgerink JD Self-Assembling Multidomain Peptide Fibers with Aromatic Cores. Biomacromolecules 2013, 14, 1370–1378. [PubMed: 23480446]

(38). Oh S; Nguyen QD; Chung K-H; Lee H Bundling of Collagen Fibrils Using Sodium Sulfate for Biomimetic Cell Culturing. ACS Omega 2020, 5, 3444–3452. [PubMed: 32118158]

(39). Li I-C; Hartgerink JD Covalent Capture of Aligned Self-Assembling Nanofibers. J. Am. Chem. Soc. 2017, 139, 8044–8050. [PubMed: 28581735]

(40). Larin KV; Sampson DD Optical Coherence Elastography - OCT at Work in Tissue Biomechanics. Biomed. Opt. Express 2017, 8, 1172–1202. [PubMed: 28271011]

(41). Viktorov IA Rayleigh and Lamb Waves: Physical Theory and Applications, 1st ed.; Springer: New York, 1967.

(42). Engler AJ; Sen S; Sweeney HL; Discher DE Matrix Elasticity Directs Stem Cell Lineage Specification. Cell 2006, 126, 677–689. [PubMed: 16923388]

(43). Yang Y; Wang K; Gu X; Leong KW Biophysical Regulation of Cell Behavior-Cross Talk between Substrate Stiffness and Nanotopography. Engineering 2017, 3, 36–54. [PubMed: 29071164]

(44). Prevedel R; Diz-Muñoz A; Ruocco G; Antonacci G. Brillouin Microscopy: An Emerging Tool for Mechanobiology. Nat. Methods 2019, 16, 969–977. [PubMed: 31548707]

(45). Taylor PM; Batten P; Brand NJ; Thomas PS; Yacoub MH The Cardiac Valve Interstitial Cell. Int. J. Biochem. Cell Biol. 2003, 35, 113–118. [PubMed: 12479860]

(46). Puperi DS; Balaoing LR; O'Connell RW; West JL; Grande-Allen KJ 3-Dimensional Spatially Organized PEG-Based Hydrogels for an Aortic Valve Co-Culture Model. Biomaterials 2015, 67, 354–364. [PubMed: 26241755]

(47). Rutkovskiy A; Malashicheva A; Sullivan G; Bogdanova M; Kostareva A; Stensløkken K-O; Fiane A; Vaage J Valve Interstitial Cells: The Key to Understanding the Pathophysiology of Heart Valve Calcification. J. Am. Heart Assoc. 2017, 6, No. e006339. [PubMed: 28912209]

(48). Liu H; Chansoria P; Delrot P; Angelidakis E; Rizzo R; tsche D; Applegate LA; Loterie D; Zenobi-Wong M Filamented Light (FLight) Biofabrication of Highly Aligned Tissue-Engineered Constructs. Adv. Mater. 2022, 34, No. e2204301. [PubMed: 36095325]

(49). Luo Z; Tang G; Ravanbakhsh H; Li W; Wang M; Kuang X; Garciamendez-Mijares CE; Lian L; Yi S; Liao J; Xie M; Guo J; Zhou Z; Zhang YS Vertical Extrusion Cryo(Bio)Printing for Anisotropic Tissue Manufacturing. Adv. Mater. 2022, 34, No. e2108931. [PubMed: 34935203]

(50). Lepzelter D; Bates O; Zaman M Integrin Clustering in Two and Three Dimensions. Langmuir 2012, 28, 5379–5386. [PubMed: 22204631]

(51). Changede R; Xu X; Margadant F; Sheetz MP Nascent Integrin Adhesions Form on All Matrix Rigidities after Integrin Activation. Dev. Cell 2015, 35, 614–621. [PubMed: 26625956]

(52). Cheng B; Wan W; Huang G; Li Y; Genin GM; Mofrad MRK; Lu TJ; Xu F; Lin M Nanoscale Integrin Cluster Dynamics Controls Cellular Mechanosensing via FAKY397 Phosphorylation. Sci. Adv. 2020, 6, No. eaax1909. [PubMed: 32181337]

(53). Baker BM; Trappmann B; Wang WY; Sakar MS; Kim IL; Shenoy VB; Burdick JA; Chen CS Cell-Mediated Fibre Recruitment Drives Extracellular Matrix Mechanosensing in Engineered Fibrillar Microenvironments. Nat. Mater. 2015, 14, 1262–1268. [PubMed: 26461445]

(54). Wang WY; Davidson CD; Lin D; Baker BM Actomyosin Contractility-Dependent Matrix Stretch and Recoil Induces Rapid Cell Migration. Nat. Commun. 2019, 10, No. 1186. [PubMed: 30862791]

(55). Wang WY; Pearson AT; Kutys ML; Choi CK; Wozniak MA; Baker BM; Chen CS Extracellular Matrix Alignment Dictates the Organization of Focal Adhesions and Directs Uniaxial Cell Migration. APL Bioeng. 2018, 2, No. 046107. [PubMed: 31069329]

(56). Ray A; Slama ZM; Morford RK; Madden SA; Provenzano PP Enhanced Directional Migration of Cancer Stem Cells in 3D Aligned Collagen Matrices. Biophys. J. 2017, 112, 1023–1036. [PubMed: 28297639]

(57). Zvietcovich F; Larin KV Wave-Based Optical Coherence Elastography: The 10-Year Perspective. Prog. Biomed. Eng. 2022, 4, No. 012007.

(58). Zvietcovich F; Rolland JP; Yao J; Meemon P; Parker KJ Comparative Study of Shear Wave-Based Elastography Techniques in Optical Coherence Tomography. J. Biomed. Opt. 2017, 22, No. 035010.

(59). Kim E; Ehrmann K Refractive Index of Soft Contact Lens Materials Measured in Packaging Solution and Standard Phosphate Buffered Saline and the Effect on Back Vertex Power Calculation. Contact Lens Anterior Eye 2020, 43, 123–129. [PubMed: 31870595]

(60). Zevallos-Delgado C; Mekonnen TT; Zvietcovich F; Singh M; Aglyamov S; Larin K Assessing Porcine Iris Elasticity and Mechanical Anisotropy with Optical Coherence Elastography. J. Biomed. Photonics Eng. 2021, 7, No. 040304.

(61). Scarcelli G; Pineda R; Yun SH Brillouin Optical Microscopy for Corneal Biomechanics. Invest. Ophthalmol. Visual Sci. 2012, 53, 185–190. [PubMed: 22159012]

(62). Balaoing LR; Post AD; Liu H; Minn KT; Grande-Allen KJ Age-Related Changes in Aortic Valve Hemostatic Protein Regulation. Arterioscler., Thromb., Vasc. Biol. 2014, 34, 72–80. [PubMed: 24177329]

(63). Stephens EH; Carroll JL; Grande-Allen KJ The Use of Collagenase III for the Isolation of Porcine Aortic Valvular Interstitial Cells: Rationale and Optimization. J. Heart Valve Dis. 2007, 16, 175–183. [PubMed: 17484468]

(64). Püspöki Z; Storath M; Sage D; Unser MTransforms and Operators for Directional Bioimage Analysis: A Survey. In Focus on Bio-Image Informatics; Springer, 2016; Vol. 219, pp 69–93.

(65). Berens P CircStat: A MATLAB Toolbox for Circular Statistics. J. Stat. Software 2009, 31, 1–21.

(66). Ahrens JH; Uzel SGM; Skylar-Scott M; Mata MM; Lu A; Kroll KT; Lewis JA Programming Cellular Alignment in Engineered Cardiac Tissue via Bioprinting Anisotropic Organ Building Blocks. Adv. Mater. 2022, 34, No. e2200217. [PubMed: 35451188]

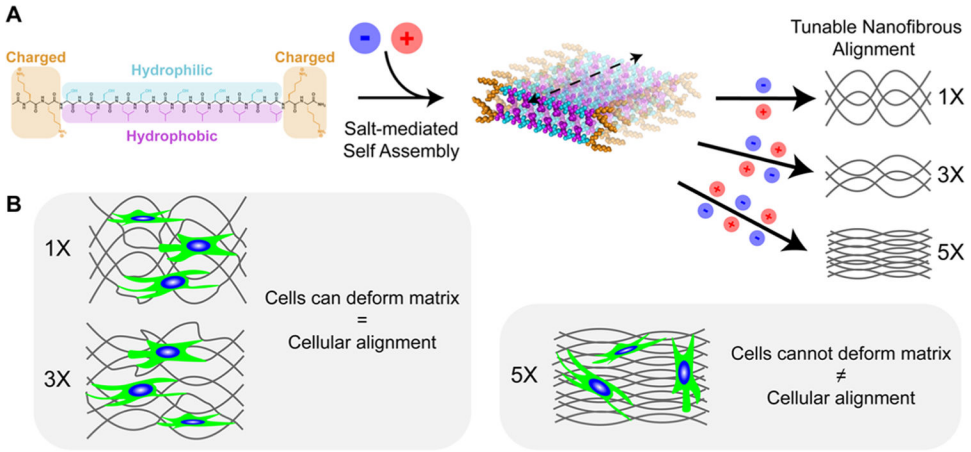

Figure 1.

K2 assembly and cellular spreading schematic. (A) K2 structure, with charged (orange), hydrophilic (blue), and hydrophobic (purple) amino acids color-coded. Salt-mediated β-sheet formation allows for tunable nanofibrous alignment. (B) Summary of cellular behavior on differentially aligned K2 matrices.

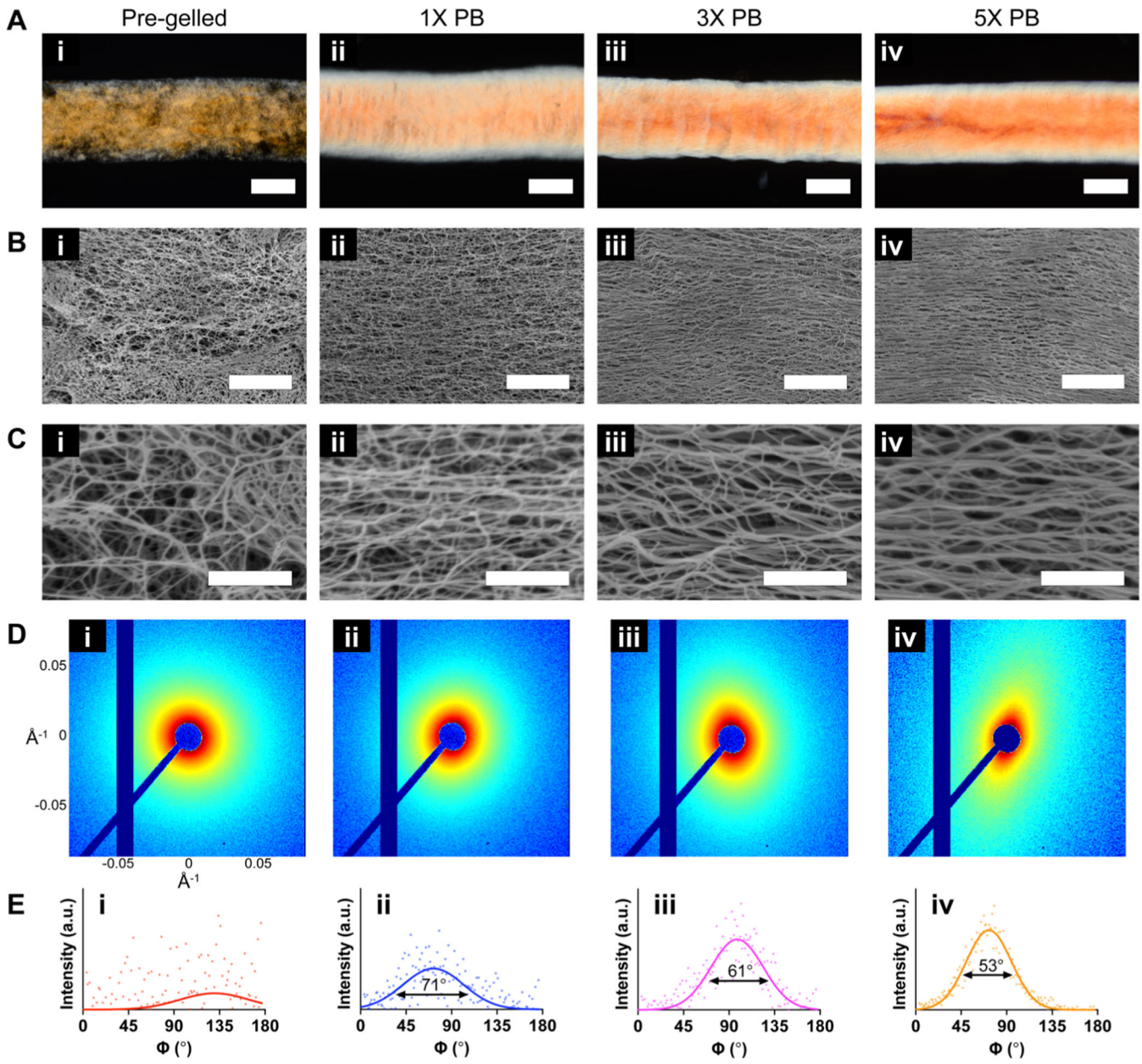

Figure 2.

Tunable alignment of nanofibrous K2 hydrogels. (A) Polarized light micrographs (scale bars = 500 μm), (B, C) scanning electron micrographs (scale bars = 3 μm and 500 nm, respectively), (D) two-dimensional small-angle X-ray scattering patterns, and (E) the azimuthal distributions of (i) pre-gelled, (ii) 1× PB, (iii) 3× PB, and (iv) 5× PB hydrogels. The full width at half-maximum for the largest peak is indicated underneath the curve.

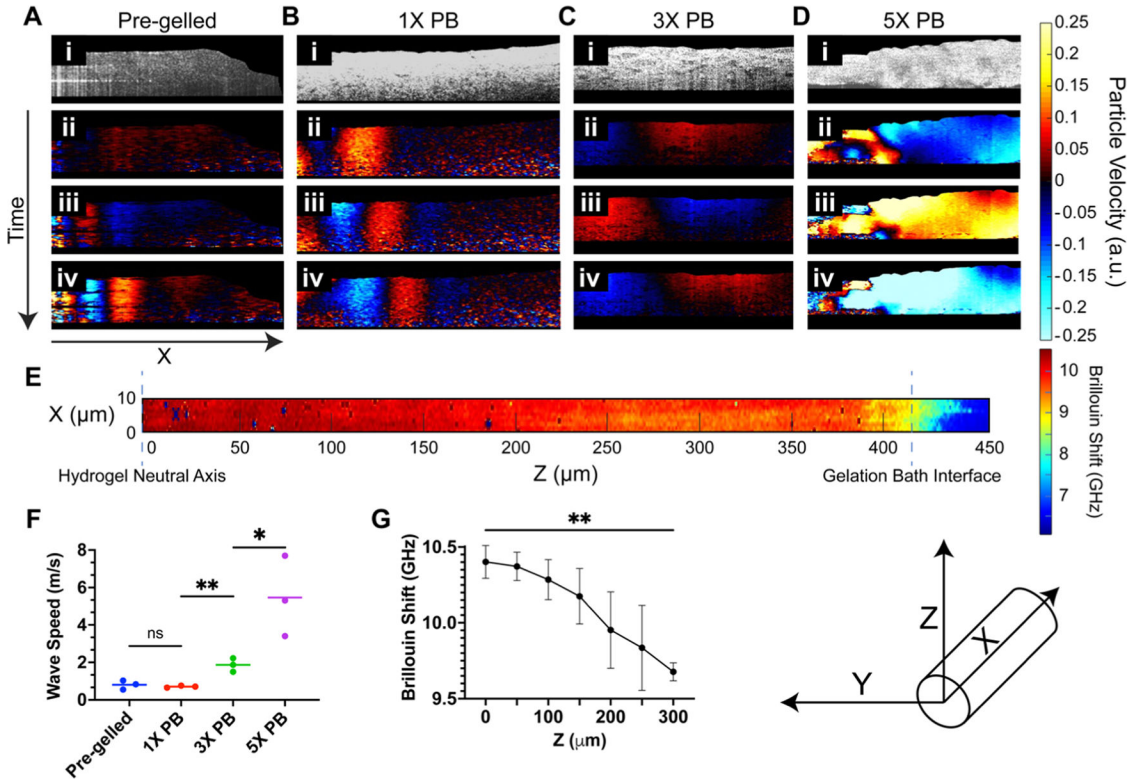

Figure 3.

Mechanical characterization of aligned K2 hydrogels. (A) Pre-gelled, (B) 1× PB, (C) 3× PB, and (D) 5× PB hydrogels. (i) Structural optical coherence tomography representations and (ii) mechanical wave snapshots at $t = 4.5$ ms, (iii) $t = 5$ ms, and (iv) 6.5 ms following a 1 kHz microtapping excitation. The color bar to the right indicates the particle velocity spectrum. (E) Brillouin shift profile for 5× PB hydrogel. The color bar to the right indicates the Brillouin shift (GHz). (F) Comparison of average wave speeds calculated using particle velocity profiles for each hydrogel type ($n = 3$ samples per condition; line at mean; $^{*}P < 0.05$, $^{**}P < 0.01$ by multiple Student's t-tests). (G) Comparison of Brillouin shift along the z-axis for 5× PB hydrogels ($n = 3$ samples with data pooled into 50 μm groupings; mean ± standard deviation; $^{**}P < 0.01$ by Student's t-test).

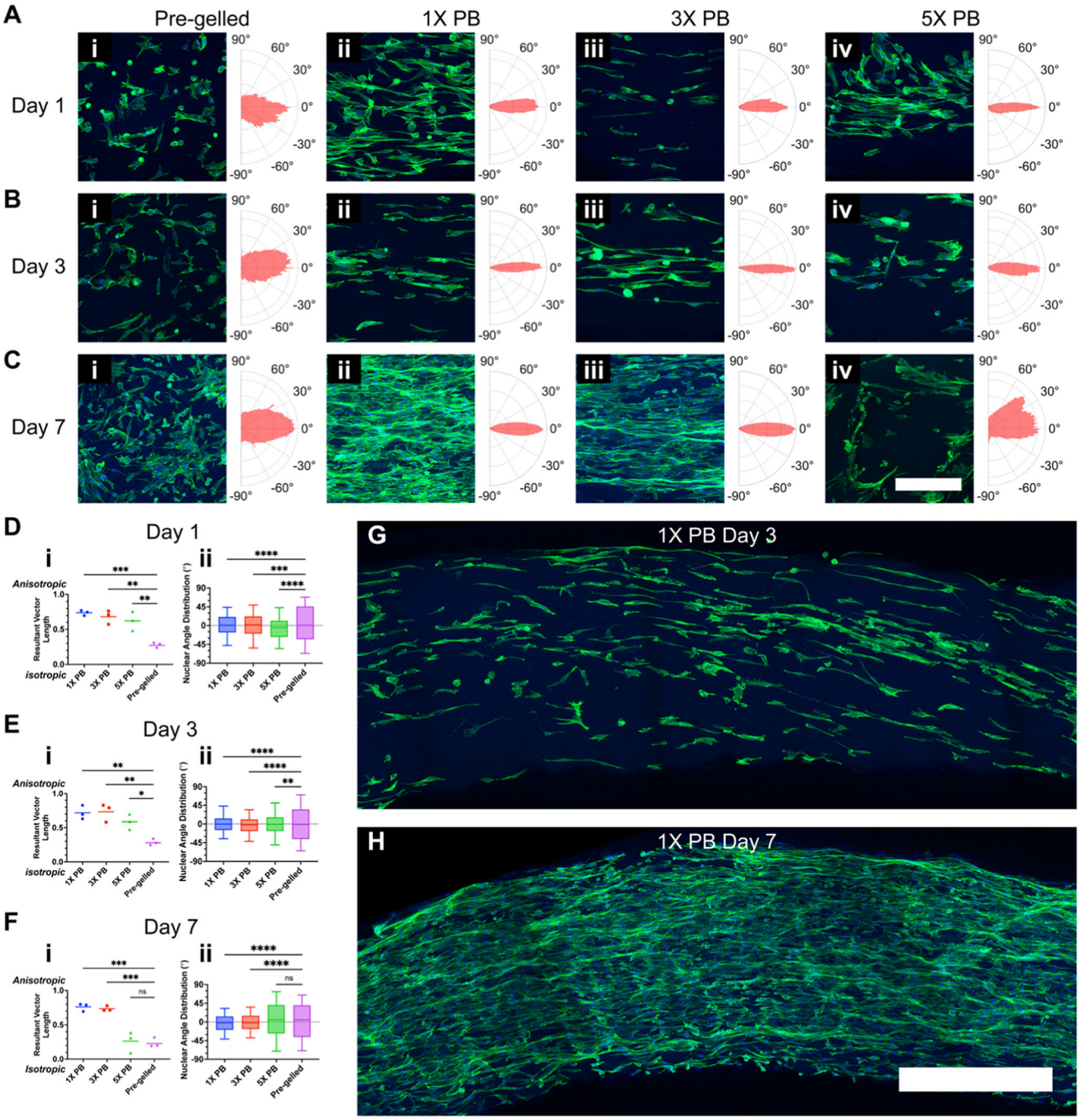

Figure 4.

Valvular interstitial cell spreading on aligned K2 hydrogels. (A) Day 1, (B) day 3, and (C) day 7 confocal microscopy images of VICs on (i) pre-gelled, (ii) 1× PB, (iii) 3× PB, and (iv) 5× PB hydrogels (DAPI = blue, F-actin = green; scale bars = 300 μm). All images are maximum intensity projections of Z-stacks that have been cropped and rotated so the direction of K2 fibrous alignment is horizontal. Polar histograms to the right of each image display the Fourier gradient structure tensor calculated using the F-actin channels, where the direction of K2 fibrous alignment is 0°. (D) Day 1, (E) day 3, and (F) day 7 comparisons of

(i) resultant vector lengths calculated from Fourier gradient structure tensors ($n = 3$ images; line at mean; *$P < 0.05$, **$P < 0.01$, ***$P < 0.001$ by one-way ANOVA and Dunnett's multiple comparison tests) and (ii) nuclear angle distributions with respect to the angle of K2 fibrous alignment ($n = 3$ images with between 294 and 1854 pooled nuclei; center line, box bounds, and whiskers indicate the median, first and third quartiles, and 10 and 90 percentiles, respectively; **$P < 0.01$, ***$P < 0.001$, ****$P < 0.0001$ by Kolmogorov–Smirnov test). (G) Day 3 and (H) day 7 confocal microscopy image stitches of VICs on 1× PB hydrogels (DAPI = blue, F-actin = green; scale bar = 500 μm).

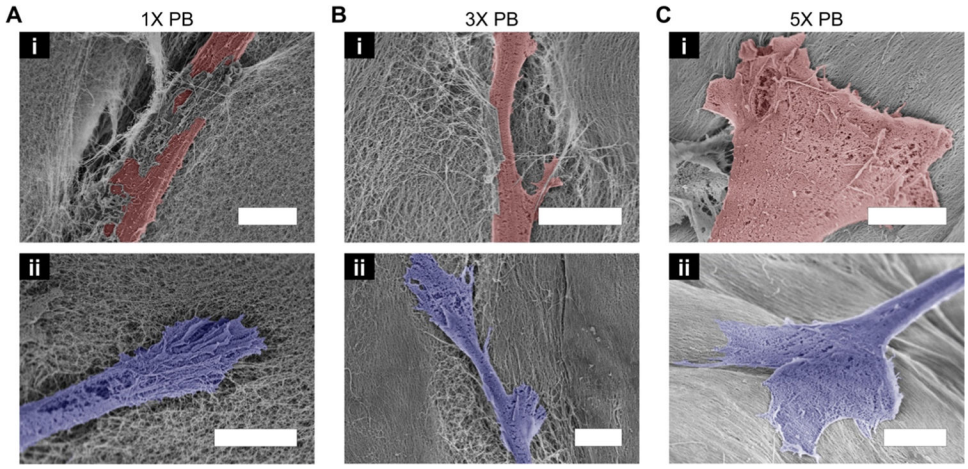

Figure 5.

Cell–matrix interactions on aligned K2 scaffolds. (A) 1× PB, (B) 3× PB, and (C) 5× PB hydrogel matrices with (i) C2C12 and (ii) VICs observed via SEM (scale bars = 5 μm). C2C12 and VIC cells are falsely colored red and blue, respectively.